Editors' Suggestion

Master-Equation Study of Quantum Transport in Realistic Semiconductor Devices Including Electron-Phonon and Surface-Roughness Scattering

Pratik B. Vyas,[1,*] Maarten L. Van de Put,[2] and Massimo V. Fischetti[2]

[1] *Department of Electrical and Computer Engineering, The University of Texas at Dallas, 800 W. Campbell Rd., Richardson, Texas 75080, USA*

[2] *Department of Materials Science and Engineering, The University of Texas at Dallas, 800 W. Campbell Rd., Richardson, Texas 75080, USA*

(Received 25 July 2019; revised manuscript received 1 October 2019; published 31 January 2020)

We study ballistic and dissipative quantum transport of electrons in realistic semiconductor devices. Ballistic electron transport is modeled by solving self-consistently the Schrödinger and Poisson equations in the two-dimensional plane of the device using the effective-mass approximation. The quantum transmitting boundary method (QTBM) is used to enforce *open* boundary conditions. Regarding dissipative transport, contrary to the widely used quantum simulations based on the nonequilibrium Green's function (NEGF) or the Wigner-function method, we model scattering using the Pauli master equation. This density-matrix-based formalism allows us to describe efficiently electronic transport—also accounting for realistic inelastic scattering processes—in semiconductor devices of sizes comparable to the electron wavelength. To this end, we analyze theoretically the impact of electron-phonon and surface-roughness scattering in silicon ultrathin-body (UTB) double-gate FETs. Our simulations show that electron transport is mainly dissipative even in devices with such small active regions. Of particular note is the predominant impact of surface-roughness scattering in UTB devices. Our calculations are consistent with the observation that scattering with surface roughness is the major factor limiting the scaling of CMOS devices.

DOI: 10.1103/PhysRevApplied.13.014067

I. INTRODUCTION

Traditionally, the theoretical analysis of realistic semiconductor devices has been done through simulation of electron transport by semiclassical methods based on the Boltzmann transport equation (BTE) [1–4] or moments of the BTE, such as the drift-diffusion [5] or the hydrodynamics model [6]. However, with the continual scaling of CMOS technology, the current and emerging generation of transistors have active regions that are smaller than the wavelength of an electron. At such small dimensions, the basic assumptions of the BTE, that electrons are highly localized "pointlike" objects with a defined position and momentum, falls short. Moreover, some of the aggressive targets set by the International Roadmap for Devices and Systems (IRDS) [7] for the silicon (Si) semiconductor industry can only be achieved by integrating explicit quantum behavior into the models used to study device performance. A full quantum-mechanical study of electron transport is therefore useful to simulate and effectively understand the behavior of modern semiconductor devices.

Widely used methods to study quantum transport include the Wigner-function method [8–10] and the nonequilibrium Green's function (NEGF) method [11–13]. While accurate *in principle*, these methods are numerically extremely expensive when attempting to account for scattering processes. Indeed, accounting for nonlocal inelastic scattering (with matrix elements that correctly include their dependence on the transfer wave vector **q**) using the NEGF formalism has been done only in very small systems [14], in Si nanowires [15], or using local (that is, **q**-independent approximations for the matrix elements) approximations for electron-phonon scattering [16]. These studies deal *only* with one-dimensional (1D) transport. The reasons are explained clearly by Lake *et al.* [16], who show that accounting for inelastic scattering within the NEGF formalism requires the inversion of a large and dense scattering-self-energy matrix. Three-dimensional (3D) NEGF simulations of dissipative quantum transport presented by Luisier *et al.* [17] or Gunst *et al.* [18] have also deployed various approximations (ignoring nonlocal effects or using the STD-Landauer method also implemented in QuantumATK [19], respectively) to get rid of the **q** dependence. The situation is even worse when dealing with the Wigner-function method. In this case, the scattering operator is simplified using simpler models [20]. Even when assuming a Boltzmann form for the scattering operator, there is a lack of studies of dissipative

*pratikvyas2008@gmail.com

 © 2020 American Physical Society

quantum transport in large two-dimensional (2D) structures using the Wigner-function method. Moreover, we should note that the situation is dire even at a formal level, since the “correct” expression for the scattering operator is intractable [21,22].

Therefore, here we follow a less conventional approach based on the Pauli master equation (PME) to treat scattering [23,24]. This Markovian class of master equations is used to describe the transition between quantum states and, thereby, the time evolution of an irreversible *open* system. In a similar fashion, the PME can be used to express the time evolution of the density matrix of a device connected to external reservoirs. Coupling between the device and reservoirs, which are assumed to be in thermal equilibrium, is established phenomenologically. Additionally, Ref. [23], following Van Hove [25], shows that for a device smaller than the phase coherence length, the injected electrons are highly delocalized and therefore the off-diagonal terms of the density matrix, which are responsible for the interference between the injected states, can be neglected. This assumption is vital to enable us to treat relatively large realistic *open* systems in a numerically efficient way. We determine the scattering states that diagonalize the density matrix by solving the Luttinger-Kohn [26] (Schrödinger) equation in the 2D plane of the device using the effective-mass approximation [27,28]. The contacts connecting the *open* system with external reservoirs are modeled using the quantum transmitting boundary method [29] (QTBM). We prefer the QTBM over NEGF-based approaches for two reasons: (1) the QTBM yields the eigenstates of our open system, which are needed for the PME, directly and (2) by exploiting the eigenstates of the contact, the QTBM is numerically more efficient than NEGF approaches [30,31]. Our technique to discretize the continuous density of states (DOS) of the *open* system accurately by exploiting the solutions of the *closed* system has a similar flavor to the method proposed in Ref. [23] and later adopted by Laux in QDAME [32,33]. The transition probabilities between the quantum states, determined using Fermi’s golden rule, are then incorporated into the PME to obtain the steady-state distribution of electrons away from the purely ballistic picture. It is important to note that we consider the system to be at steady state, even in the presence of an external force (applied bias) causing exchange of particles with the contact reservoirs. The Schrödinger equation and PME are solved self-consistently with the Poisson equation to obtain the final state of the system.

It is worth mentioning that the use of a natural basis of *open*-system wave functions in the PME allows us to include quantum-mechanical processes such as tunneling and confinement effects directly, unlike in the BTE approach. At the same time, the wave functions contain the full response to the electric field distribution in the device. Therefore, the assumption of the BTE, that the external electric field must vary slowly over the electron mean free path, is no longer required, giving us a more practical picture of the system without the semiclassical concept of pointlike electrons. Thus, the PME correctly and efficiently describes electronic transport in sub-50-nm Si-based devices, considering the fact that the electron dephasing length is of the order of 30–50 nm for Si devices at room temperature [23] with a typical doping level of 10^{21} donors/cm^2.

In short, here we wish to demonstrate an efficient method to simulate realistic devices, to highlight its significance by applying it for the case of UTB FETs with sub-10-nm gate lengths and, furthermore, to determine whether dissipation plays a significant role in the electronic transport even in the nanoscale regime. Finally, it is important to mention that the PME approach, like the other quantum methods, comes with its own set of restrictions. Since the PME uses Fermi’s golden rule, its validity is limited to cases in which the perturbation is weak. Also, by not taking into account the off-diagonal elements of the density matrix, the PME can be used only in short devices. Of course, it is also possible to account for the off-diagonal elements; however, this would result in an intractable numerical problem of a complexity similar to the inversion of the scattering self-energy matrix required by the NEGF formalism. In this paper, we study and compare the interaction of electrons with phonons and surface roughness (SR) in UTB FETs using the PME approach described above. Thus, the present work extends the theoretical formulation presented in Refs. [23] and [24] by applying the method to a realistic 2D *open* system, while at the same time implementing a nonlocal transfer-wave-vector-dependent scattering process of practical significance, namely, SR scattering.

The paper is organized as follows. Sec. II provides a detailed description of the theoretical model. An application of our model is presented in Sec. III, where we simulate the electronic behavior of UTB double-gate (DG) FETs in the dissipative picture. Finally, we draw our conclusions in Sec. IV.

II. THEORETICAL MODEL

Before delving into technical details, it is convenient to highlight some features of the numerical scheme that we employ [34]. We assign the transport, confinement, and out-of-plane directions to x, z, and y, respectively. All simulations are done in the 2D x-z plane of the device using the effective-mass approximation, limiting the calculations to the first conduction band of Si, and approximating the band minima with six equivalent ellipsoidal valleys. Translational invariance of the device profile is assumed along the out-of-plane y direction, which is a good approximation for wide devices. It is important to mention that the method described in this work is not limited to 2D simulations and can be readily extended to model full 3D cases.

The device channel is taken to be oriented along the [110] direction and the dielectric-semiconductor interface is on the [100] plane, following general trends in VLSI technology. We solve the Schrödinger equation, the PME, and the Poisson equation self-consistently to determine the electrical behavior of a device. The following sections describe our approach in detail.

A. Schrödinger equation with open boundaries

We wish to describe the behavior of a system under an applied bias (drain-source voltage $V_{\rm DS}$ in this case) that can exchange particles with the environment through its contacts. To this end, the widely used QTBM [29] is employed. The source and drain contacts are idealized as infinite leads, labeled by the index s, connected to the active region of the device, as shown in Fig. 1. We intend to inject electron waves from the leads (source and drain), find their distribution inside the device, and calculate the transmission and/or reflection coefficients into other leads. Details regarding the QTBM methodology can be found in Refs. [29] and [32]. In brief, the wave functions $\Psi^{v}_{\beta,s}(\omega_s,\kappa_s)$ in lead s consist of traveling waves along ω_s, while quantum confinement in the κ_s direction gives us wave functions that are the m eigensolutions $\varphi^{s,v}_m(\kappa_s)$ (also referred to as subbands) of the 1D Schrödinger equation with a discretized energy spectrum $E^{s,v}_m$.

The wave functions $\phi^{s,v}_\beta(x,z)$ inside the device domain are obtained by solving the time-independent single-electron Luttinger-Kohn equation using the effective-mass approximation in the 2D x-z plane of the device, independently for electron injection from each lead s. The channel oriented along the [110] direction introduces off-diagonal terms in the effective-mass tensor which, in turn, result in mixed second-order derivatives being present in the Schrödinger equation. By a rotation of coordinates and some mathematical manipulation, the mixed derivatives can be removed and we obtain the following simplified

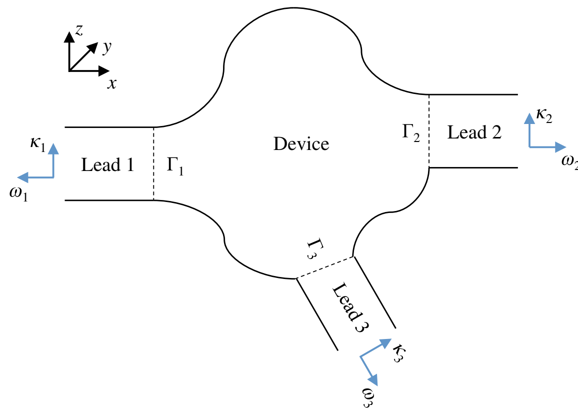

FIG. 1. A schematic illustration showing the implementation of the QTBM.

form in the plane of the device [27]:

$$-\frac{\hbar^2}{2}\left[\frac{1}{m^v_x}\frac{\partial^2\phi^{s,v}_\beta(x,z)}{\partial x^2}+\frac{1}{m^v_z}\frac{\partial^2\phi^{s,v}_\beta(x,z)}{\partial z^2}\right] + V(x,z)\phi^{s,v}_\beta(x,z) = E^v_\beta\phi^{s,v}_\beta(x,z) - \frac{\hbar^2k_y^2}{2m^v_y}\phi^{s,v}_\beta(x,z), \tag{1}$$

where V is the potential energy distribution, $1/m^v_x = \frac{1}{2}\left(1/m^v_{\rm tr}+1/m^v_{\rm op}\right)$, $1/m^v_y = 1/m^v_x - m^v_x/4\left(m^v_b\right)^2$, $1/m^v_b = 1/m^v_{\rm tr} - 1/m^v_{\rm op}$, $1/m^v_z = 1/m^v_{\rm con}$, and the full (envelope) wave function $\psi^{s,v}_\beta(x,y,z)$ can be written as

$$\psi^{s,v}_\beta(x,y,z) = e^{ik_yy}\, e^{-i(m^v_x/2m^v_b)k_yx}\phi^{s,v}_\beta(x,z). \tag{2}$$

Here, $m^v_{\rm tr}$, $m^v_{\rm con}$, and $m^v_{\rm op}$ are the effective masses in the transport, confinement, and out-of-plane directions, respectively, for a Si device channel oriented in the [100] direction. Equation (1) has to be solved for two distinct configurations, owing to the six valleys in Si and the channel orientation.

Applying the finite-difference method and incorporating the QTBM boundary conditions, Eq. (1) becomes a linear system problem:

$$\left[\mathbf{H}^D + \mathbf{\Sigma}_L + \mathbf{\Sigma}_R - E^v_\beta\,\mathbf{I}\right]\boldsymbol{\phi}^{s,v}_{m,\beta} = \mathbf{B}^m. \tag{3}$$

Here, $\mathbf{H}^D$ is the $N\times N$ Schrödinger Hamiltonian, $\mathbf{I}$ represents an $N\times N$ identity matrix, and $\mathbf{B}^m$ is an $N\times 1$ vector comprised of the traveling waves (modes) injected into the device. $\mathbf{\Sigma}_L$ and $\mathbf{\Sigma}_R$ are the $N\times N$ self-energy terms, which include the reflected and transmitted (both traveling and evanescent) waves traveling into and out of the device, respectively. Zero-value Dirichlet boundary conditions are applied at the interfaces of the computational domain through which electrons are not injected. Note that Eq. (3) can be extended beyond the effective-mass approximation to full-band models, as shown in Ref. [31]. Finally, Eq. (3) is solved for the $N\times 1$ electron wave vectors $\boldsymbol{\phi}^{s,v}_{m,\beta}$ separately for different injection energies E^v_β, traveling modes m, leads s, and conduction-band valleys v.

1. Discretization of the continuous energy spectrum

Before we can solve the *open*-system problem, an important issue that needs to be addressed is the discretization of the continuous energy spectrum E^v_β. It is convenient to use the discretization that preferentially samples the states that matter most inside the device, since the charge is determined mostly by these states. Several approaches to this problem are reported in the literature. A conventional method is to use the Dirac-delta

normalization [35] for the injected wave functions along with a corresponding 2D DOS, accounting for the infinite length of the leads. Any discretized energy set will work in this case, provided that the range extends sufficiently above the Fermi level of the device. On the contrary, the approach proposed in Ref. [23] and later adopted in QDAME [32,33] uses the "normal modes" of the device, which are standing-wave solutions of the system obtained by employing "sinelike" and "cosinelike" boundary conditions along the contact-lead interfaces, independently. We solve the "closed-system" Schrödinger equation [36] in the device domain twice, once assuming zero-value Dirichlet and once assuming Neumann boundary conditions along the device-lead interfaces, to double sample the continuous energy spectrum. The solutions (eigenfunctions) of the two *closed* systems behave as "sinelike" and "cosinelike" at the interfaces and form a complete orthogonal basis spanning the Hilbert space of physical solutions in the device that conform to the injecting boundary conditions imposed on the *open* system in equilibrium. The associated *closed*-system eigenenergies E^v_β sample the DOS correctly and are used as the injection energies for the *open* system. Even when driven out of equilibrium, the sampling technique is robust enough to discretize the continuous energy spectrum successfully and provides good convergence and accurate device solutions, the latter being verified by increasing the device size.

2. Calculation of ballistic charge

The wave functions obtained by solving the *open* system using the discretized energy spectrum obtained from the above method can be "box" normalized to the device volume [23,33], which is an added benefit of our energy-discretization scheme. Thus, the normalization is performed as follows:

$$\int_\Omega dx\, dz \left(\sum_s \sum_{m=1}^{N^v_r} |\phi^{s,v}_{m,\beta}(x,z)|^2 \right) = \frac{1}{2}. \tag{4}$$

The use of $\sum_m |\phi_m|^2$ instead of $|\sum_m \phi_m|^2$ signifies that the leads do not inject the traveling modes coherently [33]. The factor of $1/2$ is used because the energy spectrum is sampled twice by the "sinelike" and "cosinelike" *closed*-system eigenfunctions. These 2D wave functions already contain information regarding the DOS along the x and z directions. So, in order to determine the electron density, we only have to use the 1D DOS representing the continuous energy spectrum along the "homogenous" out-of-plane y direction, given by the expression

$$D^v_{\rm 1D}(E_y) = \frac{1}{\pi\hbar}\sqrt{\frac{m^v_y}{2E_y}}, \tag{5}$$

where $E_y = \hbar^2 k_y^2/2m^v_y$. The electron density $n(x,z)$ in the ballistic picture can then be calculated by associating with each wave function an occupancy factor along with the 1D DOS given by Eq. (5) and summing over all possible traveling modes for all possible injection states:

$$n(x,z) = \sum_s \sum_v \sum_\beta \sum_m \frac{1}{\pi\hbar}\sqrt{\frac{m^v_y k_B T}{2}} \times F_{-(1/2)}\left(\frac{E^r_F - E^v_\beta}{k_B T}\right) |\phi^{s,v}_{m,\beta}(x,z)|^2, \tag{6}$$

where $F_{-(1/2)}$ is the Fermi-Dirac integral [37] of order $-1/2$. The electrons are calculated for different leads r separately using the corresponding quasi-Fermi-level E^r_F associated with the lead and then summed together. The integral $F_{-(1/2)}$ is solved numerically by using discrete k_y states, keeping in mind that they are fine enough to maintain the integrity of the numerical solution. These discretized wave vectors are employed again in Sec. II B as an index, alongside m and β, to represent the states of the system.

The hole charge distribution, $p(x,y,z)$, is calculated semiclassically using the well-known 3D DOS expression

$$p(x,z) = \frac{1}{2\sqrt{\pi}}\left(\frac{2m_h k_B T}{\pi\hbar^2}\right)^{3/2} \times F_{1/2}\left(\frac{V(x,z) - (E_F + E_g)}{k_B T}\right), \tag{7}$$

where $m_h = 0.8m_0$ is the hole effective mass, the E_g is the band-gap energy of silicon, and $F_{1/2}$ is the Fermi-Dirac integral [37] of order 1/2.

Note that the inclusion of the temperature as an input parameter in the device simulation is obtained through the temperature dependence of Eqs. (6) and (7).

B. Scattering between electronic states: Solution of PME

In an *open* system driven far from equilibrium, scattering between electronic states is a major factor that drives the system toward steady state. This section is devoted to determining the out-of-equilibrium steady-state distribution of electrons in the presence of scattering. We solve the PME using the *open*-system wave functions $\phi^{s,v}_{m,\beta}$ (considering only the nonevanescent modes). We start with the Louiville–von Neumann equation of motion for the single-electron reduced density matrix ρ of the system [23], having traced over the phonons:

$$\frac{\partial\rho(t)}{\partial t} = \frac{i}{\hbar}[\rho, H] + \left(\frac{\partial\rho}{\partial t}\right)_{\rm res}, \tag{8}$$

where the second term on the right accounts for the effect of the reservoirs. Here, H is the electron, ion, and electron-ion Hamiltonian. The density matrix ρ on the basis of the eigenstates of the Hamiltonian H can be written as

$$\rho = \sum_{m\beta k_y, m'\beta' k'_y} \rho_{m\beta k_y, m'\beta' k'_y} \left|m\beta k_y\right\rangle \left\langle m'\beta' k'_y\right|. \qquad (9)$$

As already mentioned, a general formulation of dissipative transport should include the time evolution of both the diagonal and off-diagonal terms of the density matrix. Solving the transport equation for the full density matrix is a daunting task. However, in Refs. [23] and [24], it has been shown that the off-diagonal terms of the density matrix can be ignored under certain cases that we discuss later on and Eq. (8) can be simplified to the following expression for the PME:

$$\frac{\partial \rho_{m\beta k_y}}{\partial t} = \sum_{m\beta k_y \neq m'\beta' k'_y} \Big[W_{m\beta k_y, m'\beta' k'_y}\, \rho_{m'\beta' k'_y} - W_{m'\beta' k'_y, m\beta k_y}\, \rho_{m\beta k_y} \Big] + \left(\frac{\partial \rho_{m\beta k_y}}{\partial t}\right)_{\text{res}}, \qquad (10)$$

where $W_{m\beta k_y, m'\beta' k'_y}$ represents the probability per unit time for an electron to make a transition from state $|m'\beta' k'_y\rangle$ to state $|m\beta k_y\rangle$. The symbol $\rho_{m\beta k_y}$ is used to represent the diagonal matrix element $\rho_{m\beta k_y, m\beta k_y}$ for notational simplicity.

The expression for $W_{m\beta k_y, m'\beta' k'_y}$ is given by Fermi's golden rule:

$$W_{m\beta k_y, m'\beta' k'_y} = \frac{2\pi}{\hbar} |\alpha|^2 \left|\langle m\beta k_y | H' | m'\beta' k'_y\rangle\right|^2 \times \delta\Big(E_{m\beta k_y} - E_{m'\beta' k'_y}\Big), \qquad (11)$$

where H' is defined as $H_{\text{int}} = \alpha H'$, H_{int} being the interaction Hamiltonian and α being a dimensionless constant representing the strength of the interaction. The calculation of W accounts for all intravalley and intervalley transitions. Account is made for all transitions between states injected from different leads s, also termed backscattering, which forms a major scattering mechanism for electrons. However, to avoid notational complexity, a separate "lead index" is not introduced explicitly to reflect this mechanism.

We do not go in depth into the derivation of the above equation, as Ref. [24] describes it in detail. However, it is important to mention the assumptions taken in order to obtain Eq. (10) and to understand the conditions of its validity. The off-diagonal terms of the density matrix are responsible for the quantum interference and, consequently, for the spatial compression of the injected plane waves into wave packets with a width of the order of the inelastic coherence length [23]. Devices with active regions much smaller than the dephasing length of electrons will see the incoming waves as totally delocalized and therefore the off-diagonal terms are not injected by the contacts. We assume the limiting case of contacts injecting wave functions of the form given by the QTBM. Moreover, we restrict ourselves to the weak scattering limit ($\alpha^2 \ll 1$), so that the off-diagonal terms of the density matrix are not generated within the device in the course of reaching steady state.

Under the premise that the contacts inject plane waves, the reservoir interaction term of Eq. (10) can be described phenomenologically [24]. The reservoirs attempt to restore charge neutrality by injecting electrons, with traveling-wave vectors $k^{r,v}_{m,\beta}$ through the corresponding leads r, into the states that are transmitted and absorbed by these ideal contacts. Mathematically, this can be expressed as

$$\left(\frac{\partial \rho_{m\beta k_y}}{\partial t}\right)_{\text{res}} = \frac{\hbar k^{s,v}_{m,\beta}}{m^v_x} |A^{s,v}_\beta|^2 \Big[f_{\text{FD}}(E^v_\beta + E_y) - \rho_{m\beta k_y}\Big], \qquad (12)$$

where the term outside the parentheses on the right-hand side describes the group velocity of the incident electron wave, $|A^{s,v}_\beta|^2$ is the normalization constant used for $\phi^{s,v}_{m,\beta}$, and f_{FD} is the Fermi-Dirac distribution describing the occupation of the states at thermal equilibrium in the leads.

At steady state, Eq. (10) becomes

$$\sum_{m\beta k_y \neq m'\beta' k'_y} \Big[W_{m\beta k_y, m'\beta' k'_y}\, \rho_{m'\beta' k'_y} - W_{m'\beta' k'_y, m\beta k_y}\, \rho_{m\beta k_y} \Big] = -\frac{\hbar k^{s,v}_{m,\beta}}{m^v_x} |A^{r,v}_\beta|^2 \Big[f_{\text{FD}}(E^v_\beta + E_y) - \rho_{m\beta k_y}\Big]. \qquad (13)$$

This is a linear system consisting of M such equations, where M is the total number of distinct electronic states $|m\beta k_y\rangle$ injected from all the leads or, equivalently, the rank of the diagonal density matrix. Any generic linear system solver can be used to obtain the diagonal terms of the density matrix. The following sections detail how we determine the transition probabilities W for the different scattering mechanisms considered here, namely electron-phonon and SR scattering.

1. Electron-phonon scattering

We consider intravalley and intervalley scattering processes mediated by acoustic and optical phonons using Fermi's golden rule. The transition probability for intravalley scattering from the initial state $|m'\beta' k'_y\rangle$ to the final state $|m\beta k_y\rangle$ in the presence of acoustic phonons of all possible wave vectors **q** (transfer wave vectors) and angular

frequencies ω_q can be expressed as

$$W^{\rm ac}_{m\beta k_y,m'\beta' k'_y} = \frac{2\pi}{\hbar}\sum_{k'_y}\frac{1}{L_y^2}\frac{\hbar\Delta_{\rm ac}^2 q^2}{2d_c\omega_q}\left(\langle N_q\rangle + \frac{1}{2}\pm\frac{1}{2}\right) \times \int\frac{d^3q}{(2\pi)^3}|\langle m\beta k_y|e^{i\mathbf{q}\cdot\mathbf{r}}|m'\beta' k'_y\rangle|^2 \times \delta\Big(E_{\beta,k_y} - E_{\beta',k'_y}\pm\hbar\omega_q\Big), \quad (14)$$

where $\Delta_{\rm ac}$ is the acoustic phonon deformation potential, d_c is the mass density of the crystal, $\langle N_q\rangle$ is the Bose-Einstein distribution, and the plus and minus signs refer to phonon emission and absorption, respectively. The factor of $1/L_y^2$ stems from the finite-volume normalization of the electron plane wave along y, having taken a finite device width of L_y in that direction. The $\mathbf{q}$ dependence of the interaction term adds to the complexity of the calculations. A conventional way to simplify the problem and eliminate this dependence on $\mathbf{q}$ consists in assuming the elastic, high-temperature, and equipartition approximations, while approximating the dispersion of the acoustic phonons in Si as $\omega_q = c_s q$, where c_s is the sound velocity. The final expression for the transition probability in the presence of acoustic phonons then becomes

$$W^{\rm ac}_{m\beta k_y,m'\beta' k'_y} = \frac{\Delta_{\rm ac}^2 k_B T}{2\hbar d_c c_s^2}\iint dx\,dz\left|\phi^{s,v}_{m,\beta}(x,z)\right|^2\left|\phi^{s,v}_{m',\beta'}(x,z)\right|^2 \times\sum_{k'_y}\Delta k'_y\,\delta\Big(E^v_\beta - E^v_{\beta'} + E_{k_y} - E_{k'_y}\Big), \quad (15)$$

where the summation over k'_y amounts to the DOS at $E_{k_y} = E^v_\beta - E^v_{\beta'} + E_{k_y}$. A detailed derivation is given in Appendix A.

In a similar fashion, the intravalley transition probability for processes assisted by optical phonons can be expressed as

$$W^{\rm op}_{m\beta k_y,m'\beta' k'_y} = \frac{(D_tK)^2}{2d_c\omega_{\rm op}}\left(\langle N_{\rm op}\rangle + \frac{1}{2}\pm\frac{1}{2}\right) \times\iint dx\,dz\left|\phi^{s,v}_{m,\beta}(x,z)\right|^2\left|\phi^{s,v}_{m',\beta'}(x,z)\right|^2 \times\sum_{k'_y}\Delta k'_y\,\delta\Big(E^v_\beta - E^v_{\beta'} + E_{k_y} - E_{k'_y} \pm\hbar\omega_{\rm op}\Big), \quad (16)$$

where D_tK is the optical phonon deformation potential. Equation (16) accounts for both the emission and the absorption of an optical phonon of energy $\hbar\omega_{\rm op}$, where the angular frequency $\omega_{\rm op}$ is assumed to be constant. A similar expression also describes intervalley scattering mediated by optical phonons.

The approximations made here are sufficient to provide a decent quantitative idea of the impact of electron-phonon scattering in nanoscale Si devices.

2. Surface-roughness scattering

The scattering of electrons with microscopic roughness at the dielectric-semiconductor interface can significantly affect the electronic properties of modern semiconductor devices [38,39], particularly UTB FETs, which are presented as an application of our model here. SR scattering has been modeled at different levels of approximations. A methodology commonly employed consists in performing a statistical analysis of the impact of SR scattering by explicitly introducing roughness at the dielectric interface. Electron transport is then treated by using semiclassical means based on Monte Carlo [40] and drift-diffusion [41] methods for Si FETs or NEGF [42] and tight-binding-based approaches [43] for Si nanowires or ballistic simulations based on the self-consistent solution of Schrödinger and Poisson equations for UTB FETs [38,39]. Another method [44,45] based on density-functional theory (DFT) models the effect of atomic scale roughness in strained Si inversion layers by taking the chemical nature of the interface into account explicitly. These *ab initio* models that treat roughness as geometric or atomistic modifications of the interface generally tend to be computationally expensive because of the need to simulate large statistical ensembles of sample configurations of the atomic roughness. A local empirical pseudopotential-based approach to calculate SR scattering rates has been proposed [46] that aims to achieve the physical accuracy of the *ab initio* models without the added computational cost. Also pervasive in the literature are models [47–49] that treat fluctuations of the oxide barrier at the oxide-semiconductor interface as a perturbation potential. The idea was first proposed by Ando [50] for the case of bulk Si CMOS and later extended to thin bodies [51] and SOI FETs [52,53]. We model SR scattering in UTB devices in a similar fashion to Ando [50] but we also account for the change of the wave function, an effect that can be significant when dealing with UTB devices and, thus, strong quantum confinement.

Note that unlike electron-phonon scattering, SR scattering does not cause dissipation in energy. Collisions with scatterers that do not possess internal degrees of freedom (such as interface roughness or ionized impurities but unlike phonons) are not just elastic but allow us to keep track of the phase of the scattering electrons. As such, for a given microscopic configuration of the interface roughness pattern (or of the positions of all the impurities), the process is reversible. Irreversibility or loss of coherence

only becomes a factor after averaging over several SR configurations, as is done in the *ab initio* methods [40–43], thus erasing information about each of them and rendering it impossible to "retrace" the dynamic evolution of each electron back in time. The method presented here accounts for this average by incorporating a statistical quantity, the power spectrum $\langle|\Delta_{q_x,q_y}|\rangle^2$ describing the random SR configurations, to calculate scattering rates, as shown later in Eq. (21). Henceforth, the term "dissipation" is used to mean "decoherence" (or "irreversibility"), not "energy loss," in the context of SR scattering.

We start by introducing the surface roughness as a perturbation of the potential barrier at the oxide-semiconductor interface within the first Born approximation. Let the oxide-semiconductor interfaces lie at $z = 0$ (the bottom-oxide interface) and $z = t_s$, where t_s is the semiconductor thickness. In this case, the barrier potentials due to the bottom- and top-gate oxides can be written as

$$V^T_{\rm ox}(x,y,z) = V_b\Theta(-z),$$
$$V^B_{\rm ox}(x,y,z) = V_b\Theta(z-t_s),$$

where V_b is the oxide barrier, which can typically be approximated by the band gap of the oxide. Let $\Delta^B(x,y)$ and $\Delta^T(x,y)$ represent variations of the bottom- and top-oxide interfaces, respectively, from the perfect interface plane. Therefore, the perturbing potential for SR scattering can be written as

$$\begin{aligned} V_{\rm SR} = V^B_{\rm SR} + V^T_{\rm SR} = \{&V^B_{\rm ox}[x,y,z+\Delta^B(x,y)] \\ &- V^B_{\rm ox}(x,y,z)\} + \{V^T_{\rm ox}[x,y,z+\Delta^T(x,y)] \\ &- V^T_{\rm ox}(x,y,z)\}. \end{aligned} \tag{17}$$

We assume that scattering with the top and bottom interfaces is uncorrelated and therefore can be treated separately. Assuming $L_y \to \infty$, the matrix element for scattering with the bottom-oxide interface can be expressed as

$$\begin{aligned} &\langle m\beta k_y|\, V^B_{\rm SR}\,|m'\beta' k'_y\rangle \\ &= \frac{1}{L_y}\left\{\int dx \int dy \int dz\, \phi^{s,v*}_{m,\beta}(x,z) e^{-ik_y y}\, V^B_{\rm ox}[x,y,z \right. \\ &\quad + \Delta^B(x,z)]\phi^{s,v}_{m',\beta'}(x,z)e^{ik'_y y} - \int dx \int dy \int dz \\ &\quad \left. \times\, \phi^{s,v*}_{m,\beta}(x,z)e^{-ik_y y}\, V^T_{\rm ox}(x,y,z)\phi^{s,v}_{m',\beta'}(x,z)e^{ik'_y y}\right\}. \end{aligned} \tag{18}$$

Transforming the coordinates of the first integral from z to $z' = z + \Delta^B(x,y)$ and replacing z' with z, we have

$$\begin{aligned} &\langle m\beta k_y|\, V^B_{\rm SR}\,|m'\beta' k'_y\rangle \\ &= \frac{1}{L_y}\left\{\int dx \int dy \int dz\, \phi^{s,v*}_{m,\beta}[x,z-\Delta^B(x,z)]e^{-ik_y y}\right. \\ &\quad \times V^B_{\rm ox}(x,y,z)\,\phi^{s,v}_{m',\beta'}[x,z-\Delta^B(x,z)]e^{ik'_y y} \\ &\quad - \int dx \int dy \int dz\, \phi^{s,v*}_{m,\beta}(x,z) \\ &\quad \left. \times\, e^{-ik_y y}\, V^B_{\rm ox}(x,y,z)\phi^{s,v}_{m',\beta'}(x,z)e^{ik'_y y}\right\}. \end{aligned} \tag{19}$$

This apparently simple transformation of axes is a significant step. Indeed, the scattering-matrix element is now defined in terms of a shift of the electron wave function, rather than of the potential. Ando's model neglects changes in the wave function due to SR by invoking "the electric quantum limit" for inversion layers in large semiconductor devices. However, we do not have the same liberty for the case of modern SOI and UTB devices, since any change in the boundary conditions affects the wave function significantly. Moreover, we use the complete (2D) device solutions (wave functions) to improve upon the already existing models [50–53], which consider solutions of the Schrödinger equation only along the 1D cross section of the device and plane waves elsewhere. Thus our model should provide a more realistic picture, properly taking into account the quantum confinement and other nonlocal quantum effects associated with SR scattering [39].

Expanding Eq. (19) to first order in $\phi^{r,v}_{m,\beta}$, we obtain

$$\begin{aligned} &\langle m\beta k_y|\, V^B_{\rm SR}\,|m'\beta' k'_y\rangle \\ &= -\frac{V_b}{L_y}\int dx \int dy \int_{-t_{\rm ox}}^{0} dz\,\Delta^B(x,z)e^{i(k'_y-k_y)y} \\ &\quad \times\left[\frac{\partial\phi^{r,v*}_{m,\beta}(x,z)}{\partial z}\phi^{r,v}_{m',\beta'}(x,z) + \phi^{r,v*}_{m,\beta}(x,z)\frac{\partial\phi_{m',\beta'}(x,z)}{\partial z}\right], \end{aligned} \tag{20}$$

where $t_{\rm ox}$ is the oxide thickness. The surface-roughness patterns $\Delta^B(x,z)$ are random in nature and are thought to exhibit an exponential or Gaussian autocovariance [54]. The Fourier transform of the roughness pattern $\Delta^B(x,z)$ can be taken to be equal to $\sqrt{L_xL_y}\Delta_{q_x,q_y}e^{iR(q_x,q_y)}$, $\langle|\Delta_{q_x,q_y}|\rangle^2$ being the power spectrum of the roughness (discussed in detail in Sec. III A) and $\sqrt{L_xL_y}$ is the normalization constant. The factor $e^{iR(\mathbf{q})}$ (R being a random-number generator) is the Fourier transform of white noise that is introduced to generate the random pattern of the roughness. The transition probability $W^{\rm SR}_{m\beta k_y,m'\beta' k'_y}$, as well as the scattering rates associated with SR scattering, should be

considered as being affected incoherently by the randomness of the roughness patterns. Therefore, instead of taking the absolute square of the matrix element given in Eq. (19) to determine the transition probability, we use the expectation value of the absolute square of the matrix element, which is given by

$$\left\langle \left| \langle m\beta k_y | \, V_{\rm SR}^B \, | m'\beta' k'_y \rangle \right|^2 \right\rangle = \frac{4\pi^2 V_b^2}{L_y} \int dq_x \left\langle \left| \Delta^B_{q_x, k_y - k'_y} \right|^2 \right\rangle \left| \int dx \int_{-t_{\rm ox}}^{0} dz \times \left[\frac{\partial \phi^{s,v*}_{m,\beta}(x,z)}{\partial z} \phi^{s,v}_{m',\beta'}(x,z) + \phi^{s,v*}_{m,\beta}(x,z) \times \frac{\partial \phi^{s,v}_{m',\beta'}(x,z)}{\partial z} \right] e^{iq_x x} \right|^2 . \quad (21)$$

Focusing on the limits for the integral over the transfer wave vector q_x, the maximal sampling wave vector, given by $2\pi/\Delta x$, is limited by the spacing interval Δx set by our discrete mesh. From the Nyquist theorem, the maximum wave vector (q_x) of the roughness pattern that our sampling method can capture is half of the sampling wave vector, i.e, $\pi/\Delta x$. The integral over q_x in Eq. (21) can then be performed numerically within the range $[-\pi/\Delta x, \pi/\Delta x]$. The transition probability $W^{\rm SR}_{m\beta k_y, m'\beta' k'_y}$ from the state $|m'\beta' k'_y\rangle$ to the state $|m\beta k_y\rangle$ becomes

$$W^{\rm SR}_{m\beta k_y, m'\beta' k'_y} = \frac{4\pi^2 V_b^2}{\hbar} \int_{-\pi/\Delta x}^{\pi/\Delta x} dq_x \left\langle \left| \Delta^B_{q_x, k_y - k'_y} \right|^2 \right\rangle \times \left| \int dx \int_{-t_{\rm ox}}^{0} dz \left[\frac{\partial \phi^{s,v*}_{m,\beta}(x,z)}{\partial z} \phi^{s,v}_{m',\beta'}(x,z) + \phi^{s,v*}_{m,\beta}(x,z) \frac{\partial \phi^{s,v}_{m',\beta'}(x,z)}{\partial z} \right] e^{iq_x x} \right|^2 \times \sum_{k'_y} \Delta k'_y \delta\left(E^v_\beta - E^v_{\beta'} + E_{k_y} - E_{k'_y}\right). \quad (22)$$

A similar expression can be derived for scattering with the top interface. Additional details are given in Appendix B.

3. *Electron charge density in the presence of dissipation*

Within the first Born approximation, the different scattering mechanisms that we discuss are independent of each other. Therefore their transition rates can be summed together and incorporated into the PME to determine their net impact on electron transport. The density-matrix elements $\rho_{m\beta k_y}$ obtained after solving Eq. (13) can be used to determine the electron-density distribution at steady state:

$$n(x,z) = \frac{1}{\pi} \sum_r \sum_v \sum_{\beta,m,k_y} \Delta k_y \, \rho_{m\beta k_y} \left| \phi^{s,v}_{m,\beta}(x,z) \right|^2 . \quad (23)$$

C. Poisson equation

Once the distribution of all the charge carriers—electrons, holes, and ionized dopants—is known, the Poisson equation is solved in the 2D cross section (x,z) of the device, to obtain the new potential distribution. To incorporate the electrostatic effects caused by the shift in permittivity along the dielectric-semiconductor interface correctly, we solve the generalized Poisson equation:

$$\nabla \cdot [\epsilon(x,z) \nabla V(x,z)] = e^2 [p(x,z) - n(x,z) + N_A(x,z) - N_D(x,z)], \quad (24)$$

where e is the electron charge. This is a linear system:

$$P\,\mathbf{V} = \mathbf{D}, \quad (25)$$

where P is an $N \times N$ matrix expressing the differential operators on the left-hand side of Eq. (24) and $\mathbf{V}$ and $\mathbf{D}$ are $N \times 1$ vectors expressing the potential energy and the charge distributions, respectively. The centered finite-difference method is used to discretize and solve Eq. (25). The gate potential $V_{\rm GS}$ is applied by imposing Dirichlet boundary conditions along the portion of the domain edge representing the oxide-metal interface.

A known issue [9] with solving the *open* system is the occurrence of unphysical electron depletion or accumulation at the lead-device interface, typically at high $V_{\rm DS}$. Conventional methods to tackle this problem include adjusting Fermi levels at the leads to maintain charge neutrality [9,55] or using a drifted Fermi-Dirac distribution [24,33] to achieve charge neutrality or current continuity at the leads. The latter method is physically consistent with electron transport in metallic leads or highly doped homogenous systems [55]. Here, we deal with the issue of charge imbalance by employing zero-derivative boundary conditions (Neumann) for the electrostatic potential at the contacts. This approach is used primarily since it is computationally less expensive, while concurrently keeping in mind its physical limitations. The major criticism [33] of this approach is that it forces the electric field to be zero at the contacts of a biased device, which is not a physical behavior. We perform numerical tests to show that, indeed, the use of the Neumann boundary conditions for the electrostatic potential yields results that are very similar to those obtained using the more physically consistent procedure of using a drifted Fermi distribution.

D. Self-consistent scheme

The task of solving directly the Schrödinger, PME, and Poisson equations requires a self-consistent iteration process that seldom converges in practice. In order to accelerate the convergence, instead of solving Eq. (25) directly to obtain the new potential, we use the Newton method [56] to find the first approximation to the root of the Poisson equation using the following equation:

$$\mathbf{V}_{\text{new}} = \mathbf{V}_{\text{old}} - \mathbf{J}^{-1}(\mathbf{V}_{\text{old}})(P \cdot \mathbf{V}_{\text{old}} - \mathbf{D}). \qquad (26)$$

where the Jacobian $\mathbf{J}$ is calculated using a semiclassical expression [Eq. (7)] for both the electrons and the holes.

Once we have obtained the self-consistent solutions of the *open* system and, by using the PME, determined their corresponding occupations, we can calculate different current transport parameters, namely, the transmission coefficients for electrons injected at different energies, the local density of states (LDOS), the current-density distribution, and the total drain current [27].

III. AN APPLICATION

A. Description of the device

DG MOSFETs are one of the most promising candidates for the current and near-future generation of transistors due to their immunity to short channel effects and low subthreshold slope [57,58]. Thus, they present an ideal application to demonstrate the capability of our quantum transport model. Moreover, FinFETs [59,60], an industry standard for the sub-20-nm process technology, basically function as self-aligned double-gate devices [61,62], with the top-gate oxide generally being much thicker than along the side walls. Thus the results shown here hold relevance for the latter class of devices as well.

We simulate the transport characteristics of a Si UTB DG nMOS with a 5-nm-thick and 10-nm-long lightly p-type-doped (approximately 10^{15} cm^{-3}) channel as shown in Fig. 2. Figure 3 shows the simulated (self-consistent) potential-energy profile of the device. The device dimensions are set in accordance with the end-of-2027 road-map goals set by the IRDS[7]. A symmetric 1.2-nm-thick SiO_2 gate insulator is assumed for the top and bottom gates. This assumption is consistent with the reported fabrication procedures [63,64], where a 1-nm-thick SiO_2 interface layer is grown before high-κ deposition. The exact nature of the roughness present at the Si-SiO_2 interface is still an open topic of debate. Traditionally, it has been characterized using a Gaussian autocorrelation function. However, a critical statistical study by Goodnick *et al.* [54] shows that an exponential autocovariance resembles the nature of the interface more closely. Therefore, we use this model in our calculation [Eq. (22)] for SR scattering. The power

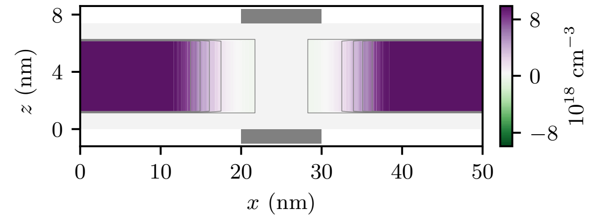

FIG. 2. The net doping profile of the simulated UTB DG nMOS. The white regions at the top and bottom represent the 1.2-nm-thick gate oxide, while the gray patches are used to highlight the positions of the gate contacts.

spectrum $\langle|\Delta_{q_x,q_y}|\rangle^2$, in this case, is given by the expression

$$\langle|\Delta_{q_x,q_y}|^2\rangle = \frac{\pi \Delta_{\text{rms}}^2 \Lambda^2}{[1 + (q_x^2 + q_y^2)\Lambda^2/2]^{3/2}}, \qquad (27)$$

where Δ_{rms} is the root-mean-square (rms) roughness, Λ is the correlation length, and $\mathbf{q}$ is the scattered wave vector, in the x-y plane, from the Fourier transform of the roughness. For this work, we take $\Delta = 0.3$ nm and $\Lambda = 1.5$ nm, following Ref. [54].

B. Simulation of different scattering phenomena

Table I lists the values of the isotropic deformation potentials Δ_{ac} and D_tK employed here to model intravalley scattering with acoustic and optical phonons, respectively, with $\hbar\omega_{\text{op}} = 60$ meV for the latter case. For intervalley scattering, we consider g- and f-type processes with optical phonons using a single-deformation-potential value in each case, which is adequate to ascertain the impact of electron-phonon scattering without going into elaborate detail. We choose to use the deformation-potential values (refer to Table I) given by Canali *et al.* [65] favoring

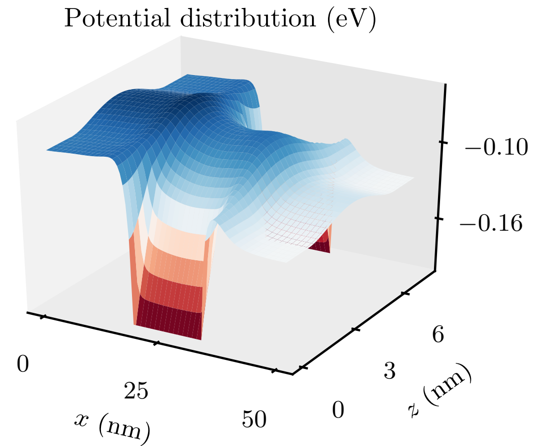

FIG. 3. The simulated potential-energy distribution in the 5-nm-thick UTB DG nMOS, plotted for reference. The potential energy is measured with respect to the source Fermi level.

TABLE I. Deformation potentials at 300 K.

Type	Symbol	Value	Units
Intravalley acoustic	Δ_{ac}	9	eV
Intravalley optical	$D_t K$	2.2×10^8	eV/cm
Intervalley f-type	$(D_t K)_f$	4×10^8	eV/cm
Intervalley g-type	$(D_t K)_g$	3×10^8	eV/cm

a weaker g-type scattering, since they have been shown [66] to correspond well with experimental mobility values for bulk and strained Si. Finally, the SR scattering rates given by Eq. (22) are inversely dependent on q and can be neglected for short wavelengths (large q) corresponding to state transitions between Si valleys. Therefore, we only consider intravalley scattering for SR.

The transition rates for the different scattering phenomena within the device domain are given by the outscattering terms $W_{m'\beta'k'_y,m\beta k_y}$ of the PME [Eq. (10)]. The total scattering rates for scattering with acoustic phonons, optical phonons, and SR, $\sum_{m'\beta'k'_y} W_{m'\beta'k'_y,m\beta k_y}$, are shown in Fig. 4 as a function of the total electron energy. The figure shows rates averaged over all states $|m\beta k_y\rangle$ with the same subband index m (represented by the different-colored lines) and injection energy E^v_β but having different k_y. These scattering rates are calculated for the individual delocalized wave functions.

Figure 4 clearly shows that the scattering rates for SR are at least an order of magnitude higher than the rates for scattering with both acoustic and optical phonons, thereby indicating a stronger impact of SR on device performance, as expected. A more quantitative discussion of the impact of this process on device performance is addressed later, in Sec. III C, when dealing with the electrical behavior of the device. Note here that the scattering rates, especially in the case of phonons, are much smaller than the reported values for bulk Si. The situation has been explicitly reported for the case of Si inversion layers in micrometer-scale MOSFETs [67]. The discrepancy arises because we take into account the overlap integral between 2D device solutions pertaining to the initial and final states when computing the corresponding transition rates, thus limiting scattering to "mutually favorable" states allowed by the device environment. From a physical point of view, the scattering rates calculated in this way account for the characteristics of the device environment—namely the electric field distribution, the carrier concentration, and the device structure, thereby presenting a more realistic picture.

Figure 6 shows the diagonal elements of the density matrix in the presence of acoustic phonons, optical phonons, and SR, separately, which gives us an idea about the final occupation of the electronic states as a function of their energy $E_{m\beta k_y}$. The solid lines represent the ballistic distribution, while the colored dots represent the distribution in the presence of different scattering mechanisms for injections from both the source and drain. A considerable shift can be seen in the final occupation of a state injected from the source and/or the drain when compared with the ballistic occupation controlled by the Fermi level of the corresponding electrode (drain and/or source). This shows that backscattering is the dominant mechanism of dissipation (loss of coherence) in all the cases presented.

C. Transport characteristics

In this section, we investigate the impact of the different scattering mechanisms on the transport behavior of the FETs that we consider. The LDOS in the device is given by the energy-resolved local probability density. The LDOS is an important tool for analyzing the device behavior. At the same time, we incorporate the occupation factors determined by the PME into the LDOS to obtain the energy-resolved electron density. This helps us to understand how the different scattering mechanisms affect the electron distribution in the device. The energy-resolved electron density, plotted in Fig. 5, resembles the spectral function commonly used in NEGF calculations. The expected broadening and/or smearing in energy of the electronic states in the presence of dissipation can be clearly seen from these plots. Backscattering of electrons results in the build-up of space charge in the channel of the device. As a result, the potential-energy in the channel is higher in the presence of scattering than in the ballistic case. This can be seen in Fig. 5, where the dashed lines represent the potential-energy distribution along the middle of the device.

Moreover, semiclassical physical observables such as the kinetic energy and drift velocity of electrons—the main information provided by Monte Carlo simulations—can also be extracted from our simulations. To study and compare the effect of the different scattering mechanisms, a spatial dependence is assigned to the expectation value of these observables (quantum operators), following Ref. [23]. The general definition of the expectation value of an operator O can be written as

$$\langle O \rangle = \frac{1}{Z} \sum_{m\beta k_y} \rho_{m\beta k_y} \langle m\beta k_y | O | m\beta k_y \rangle, \tag{28}$$

where Z is the partition function, expressed as $\sum_{m\beta k_y} \rho_{m\beta k_y} \langle m\beta k_y | m\beta k_y \rangle$. This expression can be extended to provide an arbitrary yet useful definition of a spatially dependent expectation value of an observable O, $O(x,y)$ [23,24]:

$$O(x,y) = \frac{1}{Z} \sum_{m\beta k_y} \rho_{m\beta k_y} \langle m\beta k_y | x,z \rangle \langle x,z | O | m\beta k_y \rangle. \tag{29}$$

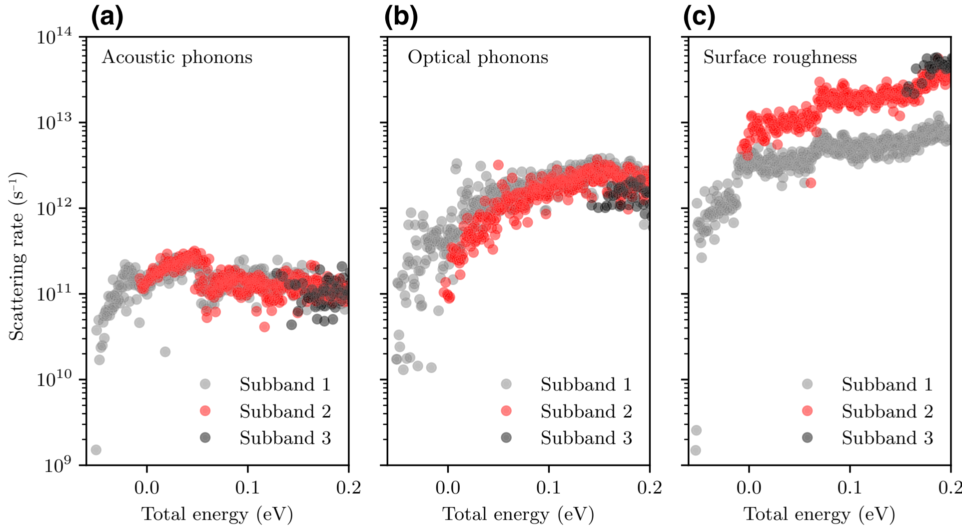

FIG. 4. Scattering rates as a function of the total electron energy simulated for the different scattering mechanisms. $V_{\mathrm{GS}} = 0.2$ V, $V_{\mathrm{DS}} = 100$ mV.

For the kinetic energy per electron E_{KE}, we then have

$$\begin{aligned} E_{\mathrm{KE}}(x,z) &= \frac{1}{Z}\sum_{m\beta k_y} \rho_{m\beta k_y}\phi^{s,v*}_{m,\beta}(x,z)\left[\frac{1}{2m_e}(-i\hbar\nabla)^2\right]\phi^{s,v}_{m,\beta}(x,z) \\ &= \frac{1}{Z}\sum_{m\beta k_y} \rho_{m\beta k_y}[E^v_\beta + E_{k_y} - V(x,z)]\left|\phi^{s,v}_{m,\beta}(x,z)\right|^2. \end{aligned} \tag{30}$$

Here, we utilize the fact that the wave functions $\phi^{s,v}_{m,\beta}$ are eigensolutions of the 2D Schrödinger equation and m_e represents the effective-mass tensor.

Figure 7 shows the kinetic energy distribution, calculated as described above, in the presence of SR scattering and its average over vertical cross sections along the device length compared with the result obtained when considering ballistic transport or scattering with only phonons. It can be seen that there is a marginal distinction in the kinetic energy for the different cases, except in the inverted-channel region. Here, the backscattering of electrons raises the potential energy, as shown in Fig. 5, and simultaneously lowers the kinetic energy in the channel.

Semiclassically, the drift velocity v_d can be viewed as $v_d = j/(\mathrm{q}_e n)$, where j is the current density and n is the carrier concentration. Extending this to the quantum regime, j transforms into the probability current given by $j = \mathrm{q}_e\hbar/m_e \,\mathrm{Re}\left(\phi^{s,v*}_{m,\beta}\nabla\phi^{s,v}_{m,\beta}\right)$. Using the semiclassical expression and following the procedure of Eq. (29), we can now define the spatially dependent expectation value of the drift velocity as

$$v_d = \frac{1}{Z}\frac{\hbar}{m_e}\sum_{m\beta k_y}\rho_{m\beta k_y}\mathrm{Re}\left[\phi^{s,v*}_{m,\beta}(x,z)\nabla\phi^{s,v}_{m,\beta}(x,z)\right], \tag{31}$$

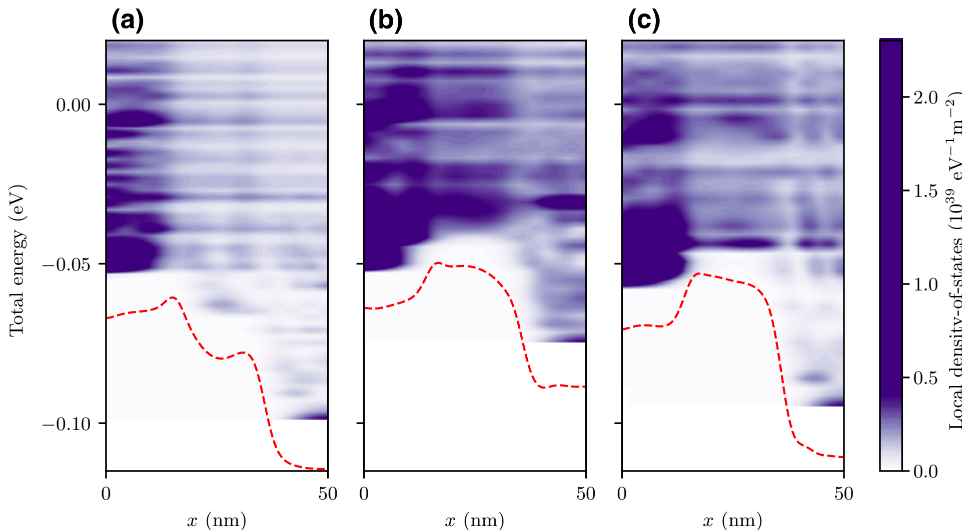

FIG. 5. The energy-resolved electron density (a) in the ballistic case, (b) in the presence of phonon (optical and acoustic) scattering, and (c) in the presence of scattering with surface roughness. The distribution is averaged over a cross-section thickness of roughly 1 nm along the middle of the device. The red dashed line represents the potential distribution cut across the device midsection. The energies are measured with respect to the source Fermi level. $V_{\mathrm{GS}} = 0.2$ V, $V_{\mathrm{DS}} = 100$ mV.

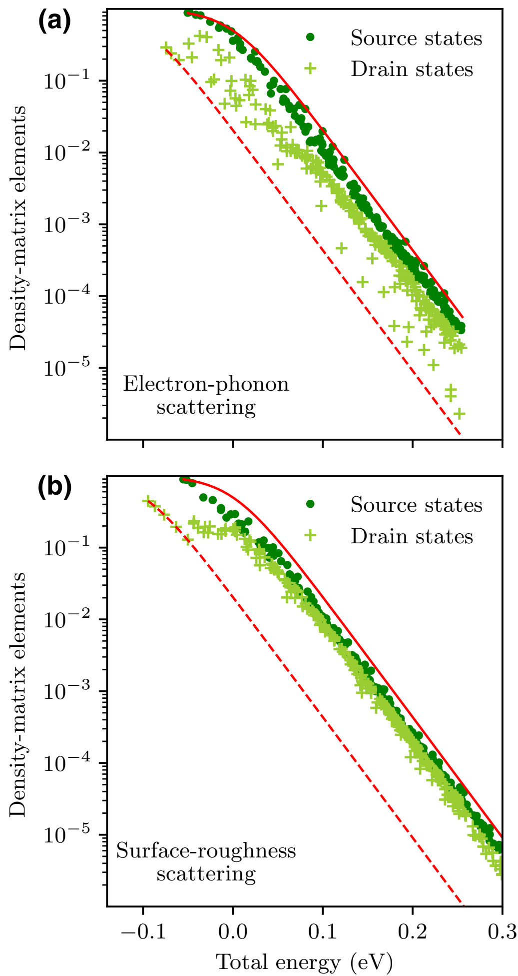

FIG. 6. The diagonal elements of the density matrix, as a function of the total electron energy, representing the final occupation of states in the presence of (a) electron-phonon scattering and (b) SR scattering. The solid and dashed red lines represent the ballistic occupation of states injected from the source and the drain, respectively.

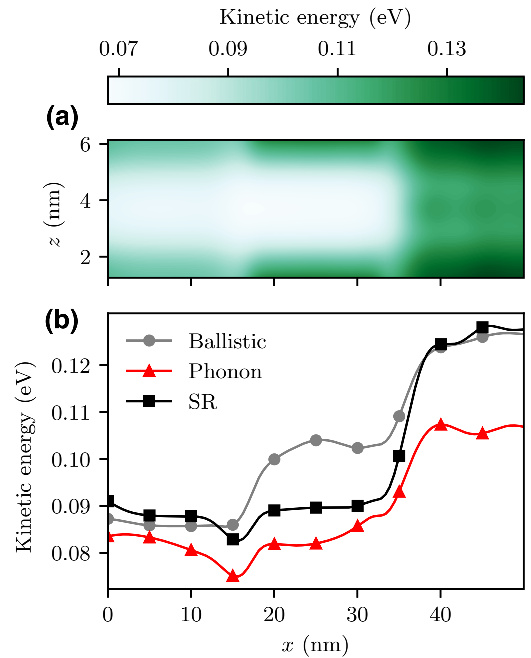

FIG. 7. (a) The spatial distribution of the electron kinetic energy in the presence of SR scattering. The kinetic energy distributions for the ballistic and electron-phonon scattering are largely similar to the above, except in the channel. The latter is highlighted in (c), which shows the kinetic energy averaged over the cross-section thickness along the length of the device for the different scattering mechanisms.

where the partition function Z acts as the quantum equivalent of the carrier concentration n. Our calculations are limited to the x-z plane of the device, since this is the region of interest. Figures 8(a) and 8(b) compare the drift-velocity distributions when accounting for scattering with phonons and SR, respectively. We can observe that there is a stark decrease in the drift velocity in the presence of surface roughness as compared to the phonons case and also the ballistic situation displayed in the comparison plot of Fig. 8(c). At the same time, Fig. 8(b) shows that transport is affected mostly near the semiconductor-dielectric interface, highlighting the interfacial nature of SR scattering [39].

Finally, we study the transfer characteristics of the device in the presence of the different scattering mechanisms. We obtain a clear quantitative assessment of the negative impact of surface roughness in UTB devices from the *on*-state behavior highlighted in Fig. 9(a). The subthreshold characteristics, as can be seen from Fig. 9, remain relatively unaffected. Interestingly, there is also a notable decrease in the drain current in the presence of scattering with phonons even in devices of such small dimensions. However, scattering with surface roughness dominates among the dissipative processes and is the principal factor limiting device performance. Comparing our results with statistical *ab initio* simulations of SR in similar device structures [38,39], we see a much more pronounced impact of SR, primarily because we explicitly take into account the 2D nature of the interface, contrary to a purely 1D [39] or a projected 1D [38] roughness pattern assumed in the cited works. Moreover, this leads to the inclusion of transitions between states having different momenta or k_y in the out-of-plane direction, while the *ab initio* cases, mentioned above, implicitly assume conservation of this out-of-plane momentum, thus limiting the scattering of electrons.

Classically, the minimum cross-section width of the "roughened" device would bottleneck the amount of the carriers flowing through the device and thus should be the parameter that determines the final current. In our case, with SR present at both the top- and bottom-oxide interfaces, this will be $(5 - 2 \times \Delta) \approx 4.4$ nm. However,

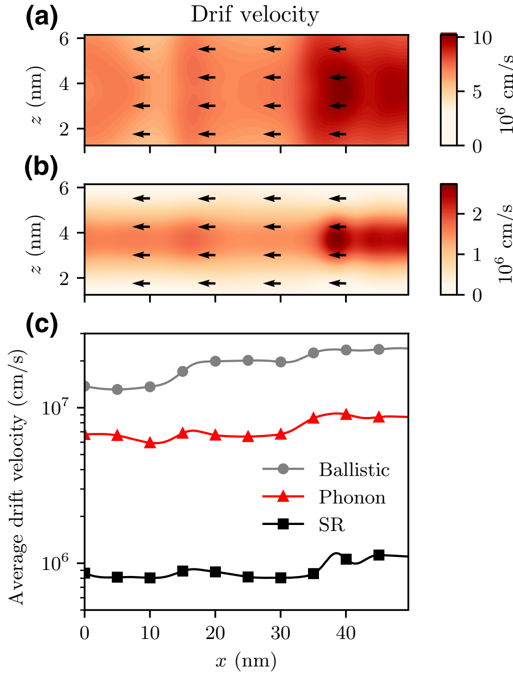

FIG. 8. The spatial distribution of the electron drift velocity in the presence of (a) electron-phonon scattering and (b) SR scattering. (c) A comparative plot of the drift velocity, averaged over the cross-section thickness along the length of the device, in the presence of different scattering mechanisms.

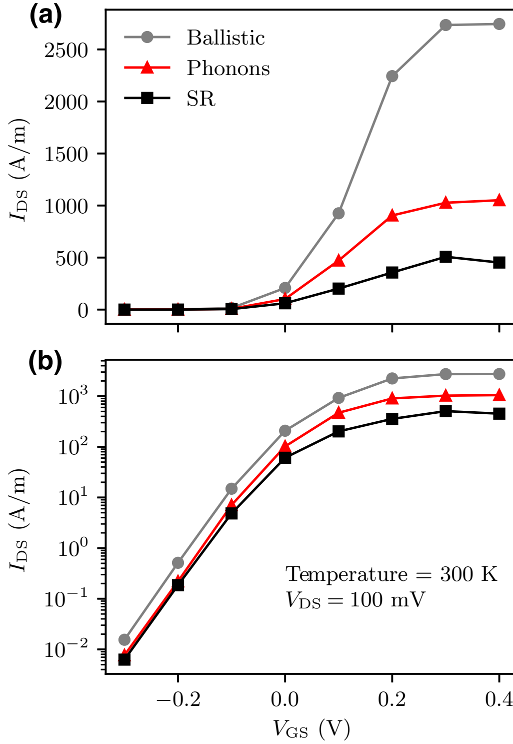

FIG. 9. The transfer characteristics of the simulated 5-nm UTB DG nMOS in (a) linear and (b) semilog scale focusing on the above-threshold and subthreshold regions, respectively.

the cross-section width required to reproduce our SR result classically is roughly a factor of 4 smaller, as can be realized if we scale our ballistic device solution linearly to match the currents in the presence of SR. This discrepancy shows the predominant role played by quantum confinement effects associated with SR, which in effect cause further constrictions of the channel.

IV. CONCLUSION

We develop a method based on the PME to treat dissipative quantum transport in realistic semiconductor devices, retaining the full nonlocality and transfer-wave-vector dependence of the scattering processes. As an application of our method, the impact of electron-phonon and SR scattering is studied for UTB FETs. The methodology can be readily extended to incorporate other scattering mechanisms, such as electron-electron and impurity scattering [68]. An extension of Ando's model is described to properly include quantum confinement and nonlocal effects associated with surface roughness. Our results show that, even in nanoscale devices, electron transport is predominantly dissipative (nonballistic). In particular, scattering of electrons with surface roughness is the prime source of dissipation, drastically reducing the drain current (ballistic) by almost an order of magnitude.

APPENDIX A: DERIVATION OF ELECTRON-PHONON SCATTERING RATES

Applying the equipartition and the elastic approximations to Eq. (14), we obtain

$$W^{\mathrm{ac}}_{m\beta k_y,m'\beta' k'_y} = \sum_{k'_y} \frac{\pi}{L_y^2}\frac{\Delta_{\mathrm{ac}}^2 k_B T}{\hbar d_c c_s^2}\int\frac{d^3q}{(2\pi)^3}\int d^3r\int d^3r'\,\psi^{s,v*}_{m,\beta}(\mathbf{r}) \times \psi^{s,v}_{m,\beta}(\mathbf{r}')e^{i\mathbf{q}(\mathbf{r}-\mathbf{r}')}\psi^{s,v}_{m',\beta'}(\mathbf{r})\psi^{s,v*}_{m',\beta'}(\mathbf{r}')\delta\left(E_{\beta,k_y}-E_{\beta',k'_y}\right).$$

Integrating over all $\mathbf{q}$, this expression can be rewritten as

$$\begin{aligned} W^{\mathrm{ac}}_{m\beta k_y,m'\beta' k'_y} &= \sum_{k'_y} \frac{\pi}{L_y^2}\frac{\Delta_{\mathrm{ac}}^2 k_B T}{\hbar d_c c_s^2}\int d^3r\int d^3r'\,\psi^{r,v*}_{m,\beta}(\mathbf{r}) \\ &\quad\times \psi^{s,v}_{m,\beta}(\mathbf{r}')e^{i\mathbf{q}(\mathbf{r}-\mathbf{r}')}\psi^{s,v}_{m',\beta'}(\mathbf{r})\psi^{s,v*}_{m',\beta'}(\mathbf{r}') \\ &\quad\times \delta\left(\mathbf{r}-\mathbf{r}'\right)\delta\left(E_{\beta,k_y}-E_{\beta',k'_y}\right) \\ &= \sum_{k'_y} \frac{\pi}{L_y^2}\frac{\Delta_{\mathrm{ac}}^2 k_B T}{\hbar d_c c_s^2}\int d^3r\left|\psi^{s,v}_{m,\beta}(\mathbf{r})\right|^2 \\ &\quad\times \left|\psi^{s,v}_{m',\beta'}(\mathbf{r})\right|^2\delta\left(E_{\beta,k_y}-E_{\beta',k'_y}\right) \end{aligned}$$

$$= \sum_{k'_y} \frac{\pi}{L_y^2} \frac{\Delta_{\rm ac}^2 k_B T}{\hbar d_c c_s^2} \int_0^{L_y} dy \iint dx\, dz \times \left|\phi^{s,v}_{m,\beta}(x,z)\right|^2 \left|\phi^{s,v}_{m',\beta'}(x,z)\right|^2 \delta\left(E_{\beta,k_y} - E_{\beta',k'_y}\right).$$

The integral over the x-z plane is only required over the device domain, since our set of *open*-system wave functions already contains information regarding the infinite leads, as discussed in Sec. II A 1. Also, assuming periodic boundary conditions along y, the wave vectors k_y can be taken as multiples as $2\pi/L_y$ and $\Delta k_y = 2\pi/L_y$. Thus, finally, we obtain the transition rate as

$$W^{\rm ac}_{m\beta k_y, m'\beta' k'_y} = \frac{\Delta_{\rm ac}^2 k_B T}{2\hbar d_c c_s^2} \iint dx\, dz \left|\phi^{s,v}_{m,\beta}(x,z)\right|^2 \left|\phi^{s,v}_{m',\beta'}(x,z)\right|^2 \times \underbrace{\sum_{k'_y} \Delta k'_y \delta\left(E^v_\beta - E^v_{\beta'} + E_{k_y} - E_{k'_y}\right)}_{\rm DOS}. \tag{A1}$$

An expression similar to Eq. (16) can also be derived for scattering, with optical phonons following a similar procedure.

APPENDIX B: DERIVATION OF SR SCATTERING RATES

The roughness pattern $\Delta^B(x,z)$ can be written as

$$\Delta^B(x,z) = \iint dq_x\, dq_y \sqrt{L_x L_y}\, \Delta_{q_x,q_y} e^{iR(q_x,q_y)} e^{iq_x x} e^{iq_y y}. \tag{B1}$$

Inserting this expression into Eq. (20) and performing the integration over y, we obtain

$$\langle m\beta k_y | V^B_{\rm SR} | m'\beta' k'_y\rangle = -\frac{2\pi V_b}{L_y} \int dx \int_{-t_{\rm ox}}^0 dz \times \left[\frac{\partial \phi^{s,v*}_{m,\beta}(x,z)}{\partial z} \phi^{s,v}_{m',\beta'}(x,z) + \phi^{s,v*}_{m,\beta}(x,z) \frac{\partial \phi^{s,v}_{m',\beta'}(x,z)}{\partial z}\right] \times \iint dq_x\, dq_y \sqrt{L_x L_y}\, \Delta_{q_x,q_y} e^{iR(q_x,q_y)} e^{iq_x x} \delta(k'_y - k_y + q_y). \tag{B2}$$

Let us define

$$\Phi(x,z) = \left[\frac{\partial \phi^{s,v*}_{m,\beta}(x,z)}{\partial z} \phi^{s,v}_{m',\beta'}(x,z) + \phi^{s,v*}_{m,\beta}(x,z) \times \frac{\partial \phi^{s,v}_{m',\beta'}(x,z)}{\partial z}\right].$$

Taking the expectation value of the square of the matrix element given by Eq. (B2), we have

$$\left\langle \left|\langle m\beta k_y | V^B_{\rm SR} | m'\beta' k'_y\rangle\right|^2 \right\rangle = \frac{4\pi^2 V_b^2 L_x}{L_y} \int dx \int dx' \int_{-t_{\rm ox}}^0 dz \int_{-t_{\rm ox}}^0 dz' \Phi(x,z) \Phi(x',z')^* \times \int dq_x \int dq_{x'} e^{iq_x x} e^{-iq'_x x'} \left\langle \Delta_{q_x,k_y-k'_y} \Delta^*_{q_{x'},k_y-k'_y}\right\rangle \times \left\langle e^{iR(q_x)} e^{iR(q'_x)}\right\rangle. \tag{B3}$$

Now, the power spectrum of white noise $\langle e^{iR(q_x)} e^{iR(q'_x)}\rangle$ is $C\delta(q_x - q'_x)$, where C is a constant. Using this fact in Eq. (B3) and taking $C = L_x$, we obtain

$$\left\langle \left|\langle m\beta k_y | V^B_{\rm SR} | m'\beta' k'_y\rangle\right|^2 \right\rangle = \frac{4\pi^2 V_b^2}{L_y} \int dq_x \times \left\langle \left|\Delta_{q_x,k_y-k'_y}\right|^2 \right\rangle \left| \int dx \int_{-t_{\rm ox}}^0 dz\, \Phi(x,z) \right|^2. \tag{B4}$$

Expressing Φ in terms of ϕ, the transition probability for SR scattering can be written as

$$W^{\rm SR}_{m\beta k_y, m'\beta' k'_y} = \frac{2\pi}{\hbar} \sum_{k'_y} \frac{4\pi^2 V_b^2}{L_y} \int dq_x \left\langle \left|\Delta_{q_x,k_y-k'_y}\right|^2 \right\rangle \times \left| \int dx \int_{-t_{\rm ox}}^0 dz \left[\frac{\partial \phi^{s,v*}_{m,\beta}(x,z)}{\partial z} \phi^{s,v}_{m',\beta'}(x,z) + \phi^{s,v*}_{m,\beta}(x,z) \frac{\partial \phi^{s,v}_{m',\beta'}(x,z)}{\partial z}\right]\right|^2 \times \delta\left(E^v_\beta - E^v_{\beta'} + E_{k_y} - E_{k'_y}\right). \tag{B5}$$

Using the same discretization for the k_ys as described in Appendix A and integrating q_x within the range $[-\pi/\Delta x, \pi/\Delta x]$, Eq. (B5) becomes

$$W^{\rm SR}_{m\beta k_y, m'\beta' k'_y} = \frac{4\pi^2 V_b^2}{\hbar} \int_{-\pi/\Delta x}^{\pi/\Delta x} dq_x \left\langle \left|\Delta^B_{q_x,k_y-k'_y}\right|^2 \right\rangle \times \left| \int dx \int_{-t_{\rm ox}}^0 dz \left[\frac{\partial \phi^{s,v*}_{m,\beta}(x,z)}{\partial z} \phi^{s,v}_{m',\beta'}(x,z) + \phi^{s,v*}_{m,\beta}(x,z) \frac{\partial \phi^{s,v}_{m',\beta'}(x,z)}{\partial z}\right] e^{iq_x x}\right|^2 \times \sum_{k'_y} \Delta k'_y \delta\left(E^v_\beta - E^v_{\beta'} + E_{k_y} - E_{k'_y}\right). \tag{B6}$$

[1] W. Kohn and J. M. Luttinger, Quantum theory of electrical transport phenomena, Phys. Rev. **108**, 590 (1957).

[2] C. Jacoboni and L. Reggiani, The Monte Carlo method for the solution of charge transport in semiconductors with applications to covalent materials, Rev. Mod. Phys. **55**, 645 (1983).

[3] M. V. Fischetti and S. E. Laux, Monte Carlo analysis of electron transport in small semiconductor devices including band-structure and space-charge effects, Phys. Rev. B **38**, 9721 (1988).

[4] J. Saint-Martin, A. Bournel, F. Monsef, C. Chassat, and P. Dolfus, Multi sub-band Monte Carlo simulation of an ultra-thin double gate MOSFET with 2D electron gas, Semicond. Sci. Technol. **21**, L29 (2006).

[5] B. Meinerzhagen and W. L. Engl, The influence of the thermal equilibrium approximation on the accuracy of classical two-dimensional numerical modeling of silicon submicrometer MOS transistors, IEEE Trans. Electron Devices **35**, 689 (1988).

[6] R. Thoma, A. Emunds, B. Meinerzhagen, H. J. Peifer, and W. L. Engl, Hydrodynamic equations for semiconductors with nonparabolic band structure, IEEE Trans. Electron Devices **38**, 1343 (1991).

[7] International Roadmap for Devices and Systems, 2017 Edition, https://irds.ieee.org/roadmap-2017.

[8] E. Wigner, On the quantum correction for thermodynamic equilibrium, Phys. Rev. **40**, 749 (1932).

[9] W. R. Frensley, Boundary conditions for open quantum systems driven far from equilibrium, Rev. Mod. Phys. **62**, 745 (1990).

[10] M. L. Van de Put, B. Sóree, and W. Magnus, Efficient solution of the Wigner-Liouville equation using a spectral decomposition of the force field, J. Comput. Phys. **350**, 314 (2017).

[11] L. P. Kadanoff and G. Baym, *Quantum Statistical Mechanics* (W. A. Benjamin, Inc., New York, 1962).

[12] L. V. Keldysh, Diagram technique for nonequilibrium processes, Zh. Eksp. Teor. Fiz. **47**, 1515 (1964).

[13] S. O. Koswatta, S. Hasan, M. S. Lundstrom, M. P. Anantram, and D. E. Nikonov, Nonequilibrium Green's function treatment of phonon scattering in carbon-nanotube transistors, IEEE Trans. Electron Devices **54**, 2339 (2007).

[14] A. Pecchia and A. Di Carlo, Atomistic theory of transport in organic and inorganic nanostructures, Rep. Progr. Phys. **67**, 1497 (2004).

[15] S. Jin, Y. J. Park, and H. S. Min, A three-dimensional simulation of quantum transport in silicon nanowire transistor in the presence of electron-phonon interactions, J. Appl. Phys. **99**, 123719 (2006).

[16] R. Lake, G. Klimeck, R. C. Bowen, and D. Jovanovic, Single and multiband modeling of quantum electron transport through layered semiconductor devices, J. Appl. Phys. **81**, 7845 (1997).

[17] M. Luisier and G. Klimeck, Atomistic full-band simulations of silicon nanowire transistors: Effects of electron-phonon scattering, Phys. Rev. B **80**, 155430 (2009).

[18] T. Gunst, T. Markussen, M. L. N. Palsgaard, K. Stokbro, and M. Brandbyge, First-principles electron transport with phonon coupling: Large scale at low cost, Phys. Rev. B **96**, 161404 (2017).

[19] S. Smidstrup *et al.*, QUANTUMATK: An integrated platform of electronic and atomic-scale modelling tools, J. Phys.: Condens. Matter **32**, 015901 (2019).

[20] O. Jonasson and I. Knezevic, Dissipative transport in superlattices within the Wigner function formalism, J. Comput. Electron. **14**, 879 (2015).

[21] I. Knezevic and B. Novakovic, Time-dependent transport in open systems based on quantum master equations, J. Comput. Electron. **12**, 363 (2013).

[22] F. P. Heinz-Peter Breuer and F. Petruccione, *The Theory of Open Quantum Systems* (Oxford University Press, New York, 2006).

[23] M. V. Fischetti, Theory of electron transport in small semiconductor devices using the Pauli master equation, J. Appl. Phys. **83**, 270 (1998).

[24] M. V. Fischetti, Master-equation approach to the study of electronic transport in small semiconductor devices, Phys. Rev. B **59**, 4901 (1999).

[25] L. Van Hove, Quantum-mechanical perturbations giving rise to a statistical transport equation, Physica **XXI**, 517 (1954).

[26] J. M. Luttinger and W. Kohn, Motion of electrons and holes in perturbed periodic fields, Phys. Rev. **97**, 869 (1955).

[27] P. B. Vyas, C. Naquin, H. Edwards, M. Lee, W. G. Vandenberghe, and M. V. Fischetti, Theoretical simulation of negative differential transconductance in lateral quantum well nMOS devices, J. Appl. Phys. **121**, 044501 (2017).

[28] P. B. Vyas, M. L. Van de Put, and M. V. Fischetti, in *2018 International Conference on Simulation of Semiconductor Processes and Devices (SISPAD)* (Austin, TX, 2018), p. 1.

[29] C. S. Lent and D. J. Kirkner, The quantum transmitting boundary method, J. Appl. Phys. **67**, 6353 (1990).

[30] S. Brück, M. Calderara, M. H. Bani-Hashemian, J. VandeVondele, and M. Luisier, Efficient algorithms for large-scale quantum transport calculations, J. Chem. Phys. **147**, 074116 (2017).

[31] M. L. Van de Put, M. V. Fischetti, and W. G. Vandenberghe, Scalable atomistic simulations of quantum electron transport using empirical pseudopotentials, Comp. Phys. Comm. **244**, 156 (2019).

[32] S. E. Laux, A. Kumar, and M. V. Fischetti, Ballistic FET modeling using QDAME: Quantum device analysis by modal evaluation, IEEE Trans. Nanotechnol. **1**, 255 (2002).

[33] S. E. Laux, A. Kumar, and M. V. Fischetti, Analysis of quantum ballistic electron transport in ultrasmall silicon devices including space-charge and geometric effects, J. Appl. Phys. **95**, 5545 (2004).

[34] P. B. Vyas, Theoretical study of quantum transport in realistic semiconductor devices, Doctoral dissertation, School, The University of Texas at Dallas, 2019.

[35] J. Fang, W. G. Vandenberghe, B. Fu, and M. V. Fischetti, Pseudopotential-based electron quantum transport: Theoretical formulation and application to nanometer-scale silicon nanowire transistors, J. Appl. Phys. **119**, 035701 (2016).

[36] F. Stern, Self-consistent results for *n*-type Si inversion layers, Phys. Rev. B **5**, 4891 (1972).

[37] We use the usual definition of the Fermi-Dirac integral of order σ as: $F_\sigma(\eta) = \int_0^\infty \frac{\varepsilon^\sigma \, d\varepsilon}{1+\exp(\varepsilon-\eta)}$.
[38] A. Cresti, M. G. Pala, S. Poli, M. Mouis, and G. Ghibaudo, A comparative study of surface-roughness-induced variability in silicon nanowire and double-gate FETs, IEEE Trans. Electron Devices **58**, 2274 (2011).
[39] P. B. Vyas, M. L. Van de Put, and M. V. Fischetti, in *2018 IEEE 13th Nanotechnology Materials and Devices Conference (NMDC)* (Portland, OR, 2018), p. 1.
[40] C. Riddet, A. R. Brown, C. L. Alexander, J. R. Watling, S. Roy, and A. Asenov, 3-D Monte Carlo simulation of the impact of quantum confinement scattering on the magnitude of current fluctuations in double gate MOSFETs, IEEE Trans. Nanotechnol. **6**, 48 (2007).
[41] A. Asenov, S. Kaya, and J. H. Davies, Intrinsic threshold voltage fluctuations in decanano MOSFETs due to local oxide thickness variations, IEEE Trans. Electron Devices **49**, 112 (2002).
[42] J. Wang, E. Polizzi, A. Ghosh, S. Datta, and M. Lundstrom, Theoretical investigation of surface roughness scattering in silicon nanowire transistors, Appl. Phys. Lett. **87**, 043101 (2005).
[43] M. Luisier, A. Schenk, and W. Fichtner, Atomistic treatment of interface roughness in Si nanowire transistors with different channel orientations, Appl. Phys. Lett. **90**, 102103 (2007).
[44] M. H. Evans, X. G. Zhang, J. D. Joannopoulos, and S. T. Pantelides, First-Principles Mobility Calculations and Atomic-Scale Interface Roughness in Nanoscale Structures, Phys. Rev. Lett. **95**, 106802 (2005).
[45] G. Hadjisavvas, L. Tsetseris, and S. T. Pantelides, The origin of electron mobility enhancement in strained MOSFETs, IEEE Electron Device Lett. **28**, 1018 (2007).
[46] M. V. Fischetti and S. Narayanan, An empirical pseudopotential approach to surface and line-edge roughness scattering in nanostructures: Application to Si thin films and nanowires and to graphene nanoribbons, J. Appl. Phys. **110**, 083713 (2011).
[47] R. E. Prange and T. Nee, Quantum spectroscopy of the low-field oscillations in the surface impedance, Phys. Rev. **168**, 779 (1968).
[48] K. Moors, B. Soree, and W. Magnus, Modeling surface roughness scattering in metallic nanowires, J. Appl. Phys. **118**, 124307 (2015).
[49] E. B. Ramayya, D. Vasileska, S. M. Goodnick, and I. Knezevic, Electron transport in silicon nanowires: The role of acoustic phonon confinement and surface roughness scattering, J. Appl. Phys. **104**, 063711 (2008).
[50] T. Ando, A. B. Fowler, and F. Stern, Electronic properties of two-dimensional systems, Rev. Mod. Phys. **54**, 437 (1982).
[51] S. Jin, M. V. Fischetti, and T. W. Tang, Modeling of surface-roughness scattering in ultrathin-body SOI MOSFETs, IEEE Trans. Electron Devices **54**, 2191 (2007).
[52] T. Ishihara, K. Uchida, J. Koga, and S. Takagi, Unified roughness scattering model incorporating scattering component induced by thickness fluctuations in silicon-on-insulator metal-oxide-semiconductor field-effect transistors, Jpn. J. Appl. Phys. **45**, 3125 (2006).
[53] D. Esseni, On the modeling of surface roughness limited mobility in SOI MOSFETs and its correlation to the transistor effective field, IEEE Trans. Electron Devices **51**, 394 (2004).
[54] S. M. Goodnick, D. K. Ferry, C. W. Wilmsen, Z. Lilienthal, D. Fathy, and O. L. Krivanek, Surface roughness at the Si(100)-SiO_2 interface, Phys. Rev. B **32**, 8171 (1985).
[55] W. Pötz, Self-consistent model of transport in quantum well tunneling structures, J. Appl. Phys. **66**, 2458 (1989).
[56] G. Dahlquest and A. Bjorck, *Numerical Methods* (Prentice-Hall, Englewood Cliffs, N.J., 1974).
[57] F. Balestra, C. Cristoloveanu, M. Benachir, J. Brini, and T. Elewa, Double-gate silicon-on-insulator transistor with volume inversion: A new device with greatly enhanced performance, IEEE Electron Device Lett. **8**, 410 (1987).
[58] R. H. Yan, A. Ourmazd, and K. F. Lee, Scaling the Si MOSFET: From bulk to SOI to bulk, IEEE Trans. Electron Devices **39**, 1704 (1992).
[59] D. Hisamoto, W.-C. Lee, J. Kedzierski, E. Anderson, H. Takeuchi, K. Asano, T.-J. King, J. Bokor, and C. Hu, A folded-channel MOSFET for deep-sub-tenth micron era, IEDM Tech. Dig. **38**, 1032 (1998).
[60] D. Hisamoto, W.-C. Lee, J. Kedzierski, H. Takeuchi, K. Asano, C. Kuo, E. Anderson, T.-J. King, J. Bokor, and C. Hu, FinFET—a self-aligned double-gate MOSFET scalable to 20 nm, IEEE Trans. Electron Devices **47**, 2320 (2000).
[61] X. Huang *et al.*, Sub-50 nm p-channel FinFET, IEEE Trans. Electron Devices **48**, 880 (2001).
[62] Y.-K. Choi, N. Lindert, P. Xuan, S. Tang, D. Ha, E. Anderson, T.-J. King, J. Bokor, and C. Hu, in *International Electron Devices Meeting Technical Digest* (Washington, 2001), p. 19.1.1.
[63] V. V. Iyengar, A. Kottantharayil, F. M. Tranjan, M. Jurczak, and K. De Meyer, Extraction of the top and sidewall mobility in FinFETs and the impact of fin-patterning processes and gate dielectrics on mobility, IEEE Trans. Electron Devices **54**, 1177 (2007).
[64] M. J. H. van Dal *et al.*, in *2007 IEEE Symposium on VLSI Technology* (Kyoto, 2007), p. 110.
[65] C. Canali, C. Jacoboni, F. Nava, G. Ottaviani, and A. Alberigi-Quaranta, Electron drift velocity in silicon, Phys. Rev. B **12**, 2265 (1975).
[66] M. V. Fischetti, F. Gámiz, and W. Hänsch, On the enhanced electron mobility in strained-silicon inversion layers, J. Appl. Phys. **92**, 7320 (2002).
[67] M. V. Fischetti and S. E. Laux, Monte Carlo study of electron transport in silicon inversion layers, Phys. Rev. B **48**, 2244 (1993).
[68] M. V. Fischetti and W. G. Vandenberghe, *Advanced Physics of Electron Transport in Semiconductors and Nanostructures* (Springer International Publishing, Switzerland, 2016).